

## Article

# Study on Critical Drawdown Pressure of Sanding for Wellbore of Underground Gas Storage in a Depleted Gas Reservoir

Rui Song <sup>1</sup>, Ping Zhang <sup>2</sup>, Xiaomin Tian <sup>2</sup>, Famu Huang <sup>2</sup>, Zhiwen Li <sup>2</sup> and Jianjun Liu <sup>1,\*</sup>

<sup>1</sup> State Key Laboratory of Geomechanics and Geotechnical Engineering, Institute of Rock and Soil Mechanics, Chinese Academy of Sciences, Wuhan 430071, China

<sup>2</sup> PipeChina West East Gas Pipeline Company, Shanghai 200120, China

\* Correspondence: jjliu@whrsm.ac.cn

**Abstract:** Accurately predicting the critical differential pressure (CDP) of sand production contributes to improving the peak-shaving capacity and ensuring safe operation of underground gas storage (UGS). The CDP of sanding production in the target wells of the UGS was predicted coupling laboratory tests, inversed analysis with well logging data and numerical simulations. The in-situ mechanical properties of rock were estimated by coupling the laboratory test results and well-logging data. The in-situ stress field of the target formation was then deduced through inversed analysis coupled finite element method (FEM) and genetic algorithm (GA), based on the existing known stress data and the seismic data of the measured points. Using the critical strain limit (CSL) of 5‰ as the sanding criterion of the wellbore, the CDPs of the gas production in the UGS were predicted, which was 5.59 MPa, 3.98 MPa, and 4.01 MPa for well #1, well #2 and well #3, when the pressure of the gas storage was 30 MPa, respectively. The simulation results showed good agreements with the field-measured benchmark data of well #2 and well #3. The effects of moisture contents (ranging from 10 to ~40%), and cycling times of gas injection and withdrawal (ranging from 40 to ~200 cycling times) on the critical differential pressure were simulated and analyzed. The results indicated that the CDP decreased with an increase of the moisture content and the cycling times. This study provides a reliable tool for the sanding prediction of the wellbore in the UGS.

**Keywords:** sanding prediction; underground gas storage; depleted gas reservoir; inversed analysis; in-situ crustal stress; critical differential pressure

**Citation:** Song, R.; Zhang, P.; Tian, X.; Huang, F.; Li, Z.; Liu, J. Study on Critical Drawdown Pressure of Sanding for Wellbore of Underground Gas Storage in a Depleted Gas Reservoir. *Energies* **2022**, *15*, 5913. <https://doi.org/10.3390/en15165913>

Academic Editor: Reza Rezaee

Received: 25 July 2022

Accepted: 12 August 2022

Published: 15 August 2022

**Publisher's Note:** MDPI stays neutral with regard to jurisdictional claims in published maps and institutional affiliations.



**Copyright:** © 2022 by the authors. Licensee MDPI, Basel, Switzerland. This article is an open access article distributed under the terms and conditions of the Creative Commons Attribution (CC BY) license (<https://creativecommons.org/licenses/by/4.0/>).

## 1. Introduction

In the past half year of 2022, the world witnessed a surge in energy prices due to geopolitical conflicts and the resulting energy crisis, which highlights the urgency of building national energy reserves. Fossil fuels, including coal, oil and natural gas, have been powering economies for over hundred years, and currently supply about 80 percent of the world's energy [1–3]. Currently, underground gas storage (UGS) has been regarded as the best potential tool for the storage and peak-regulation supply to meet the load variations of natural gas (NG) [4]. There are three main types of UGS, including depleted gas reservoirs, aquifer reservoirs and salt cavern reservoirs [5]. The depleted gas reservoirs are the most common for UGS, from which the economically favorable NG has previously been produced. The high-pressure NG is injected into the reservoir and stored in pore space between grains. Depleted gas reservoirs are regarded as the most economically attractive UGS, since they could re-use the extraction and distribution infrastructure of the gas field after suitable modification to reduce the construction costs [6]. Moreover, the geological and physical characteristics of the depleted gas reservoir have already been studied and are usually well known [7,8]. The most common factors used to evaluate the UGS facility are storage facility and injection–withdrawal capacity, both of which depend on the total amount of gas in the reservoir and the operational parameters [9,10]. A higher

injection–withdrawal capacity means more NG will be stored and extracted in a short time and achieve the balance between supply and demand. However, the periodic injection and withdrawal of the gas make the pore pressure change significantly, resulting in alternating loads on the rock skeleton of the reservoir. When the differential pressure of the NG withdrawal is increased to meet for the peak shaving requirements, the effective pressure of the well bore may rise beyond the loading capacity of the rock and cause sand production. The sands in the high-speed gas will wear downhole pipe strings and production equipment, and cause failure of high-pressure processing equipment for surface gas production, plugging of the production wellbore and damage to the reservoir, and even disasters of borehole collapse and casing damage [11,12]. Thus, accurately predicting the critical differential pressure (CDP) of sand production is one of the key issues to improving the peak-shaving capacity and ensuring safe operation of UGS.

Experimental study on the sanding of the reservoir can be dated from the beginning of the petroleum industry. Many scholars studied the sanding production through the sand arching phenomenon. They used specially designed boxes filled with sands of different properties (e.g., grain size and shape [13,14], roughness [15], moisture content [16], minerals [17], compactness [17]) and investigated the evolution of the sand arching under different confining pressures [18] and different rates of fluid injection [19,20]. However, the laboratory tests were time-consuming and expensive, especially in samples preparation, and the boundary effects could not be neglected since the size of the testing sample was too small compared to engineering applications. In addition, the sand production of loosely consolidated rock was mainly studied by these experiments since it was hard to investigate the sanding phenomenon of rock with high strength, such as the rock of the UGS in a depleted gas reservoir.

The theoretical and numerical modelling of the sanding evaluations of the injection–withdrawal well in the reservoir have been studied for decades [21], and can be classified into three categories: a sanding risk evaluation index (e.g., rock properties, or operating conditions), analytical approaches, and numerical modelling of CDP [22]. The sanding risk evaluation indexes in the literature included porosity [23], acoustic log signature [24], mechanical properties (e.g., bulk modulus, shear modulus), density, or an empirical index combining some of these parameters [25–27], as listed in Table 1. These empirical indexes were simple and convenient for the estimation of the sanding risk of the target reservoir. However, these indexes were applied and validated in unconsolidated reservoirs, but usually failed in tight reservoirs. The unconsolidated reservoir is mainly composed of loose sandstone, which is characterized by weak cementation, high porosity and high permeability, low strength and strong plasticity [28]. The tight reservoir is defined using the in-situ gas permeability of 0.1 mD or less by the U.S. Federal Energy Regulatory Commission in 1970s [29]. Compared to the unconsolidated reservoir, the rock in the tight reservoir is characterized by stronger cementation, lower porosity, lower permeability, and higher strength. The critical value of indexes usually varied with the reservoir types.

**Table 1.** Index of sanding risk of reservoirs in the literature.

Sanding Index	Equation	Threshold
Porosity [23]	$\psi = \text{Volume}_{\text{pore}}/\text{Volume}_{\text{total}}$	Varying with the reservoir types; where $\text{Volume}_{\text{pore}}$ and $\text{Volume}_{\text{total}}$ are the volume of the pore and the rock, respectively.
Acoustic wave travel time [24]	$\Delta t_c = \frac{1}{V_p}$	where $V_p$ is the velocity of the P-wave; 95 $\mu\text{s}/\text{ft} < \Delta t_c < 105 \mu\text{s}/\text{ft}$ , Slight sanding; $\Delta t_c \geq 105 \mu\text{s}/\text{ft}$ , Severe sanding
Combination modulus $E_c$ [25]	$E_c = \frac{9.94 \times 10^8 \rho_r}{\Delta t_c^2}$	where $\rho_r$ is the rock density; $E_c \geq 2.0 \times 10^4 \text{ MPa}$ , No sanding; $2.0 \times 10^4 \text{ MPa} \geq E_c \geq 1.5 \times 10^4 \text{ MPa}$ , Slight sanding; $E_c < 1.5 \times 10^4 \text{ MPa}$ , Severe sanding

Index $B_i$ [26]	$B_i = K + \frac{4}{3}G$	where $K$ and $G$ are the volumetric modulus and shear modulus; $B_i > 20$ GPa, No sanding; $20 \text{ GPa} > B_i \geq 1.4 \times 10^4$ MPa, Slight sanding (but will sanding seriously after water breakthrough); $B_i < 14$ GPa, Severe sanding
Schlumberger's ratio [27]	$R = \frac{(1-2\mu) + (1+\mu)\rho^2}{6(1-\mu)(\Delta t_p)^4}$	where $\mu$ is the Poisson's ratio; $R \leq 5.9 \times 10^7$ MPa <sup>2</sup> , Sanding

In addition, these indexes only reflected the influences of the intrinsic rock properties on the sanding risk estimation, without considering the production conditions in the well. Some scholars studied the stress distribution of the wellbore after drilling, and found the yielding zone near the well zone was the main reason for the sanding during the production of the reservoir. Through assuming that the wellbore zone was homogeneous, isotropic and met the plane strain condition, the stress distribution of the wellbore was derived. Coupling with different yield criterions of rock (e.g., compressional, shear, or tensile failure), the CDP of the wellbore could be predicted [30–34], some of which are listed in Table 2. However, the analytical models can only predict the onset of sanding production with limited accuracy due to all the assumptions and simplification, and fail in considering the complexity and heterogeneity of the formation and the dynamic crustal stress and operational conditions.

**Table 2.** Analytical equation of CDP for sanding production in the literature.

CDP Model	Equation	Nomenclature	Failure Mode
Unconfined compressive strength(UCS)/2 [30]	$\Delta P_w^{cr} = L \times \sigma_{UCS}$	$L$ is the empirical constant of 0.3~0.5, $\sigma_{UCS}$ is the uniaxial compressive strength	Compressional failure
Nordgren's model [31]	$\Delta P_w^{cr} = J_2 - c\bar{J}_1$ $\bar{J}_1 = (\sigma_1 + \sigma_2 + \sigma_3) / 3 - p$ $J_2 = ([\sigma_1 - \sigma_2]^2 + [\sigma_2 - \sigma_3]^2 + [\sigma_3 - \sigma_1]^2) / 6$	$c$ is the material constant for non-linearity	
Almisdred's model [32]	$\Delta P_w^{cr} = \max \left\{ \begin{array}{l} \frac{\frac{3\mu}{1-\mu} P_{ob} - \sigma_{UCS} S^a}{2B} \\ \left( 3 - \frac{3\mu}{1-\mu} \right) \frac{P_{ob} - \sigma_{UCS} S^a}{2B} \\ \frac{\frac{\mu}{1-\mu} P_{ob} - \sigma_{UCS} S^a}{B} \end{array} \right\}$	$B$ is the Biot's constant, $P_{ob}$ is the overburden pressure, $s$ and $a$ are Hoek Brown material constants	Shear failure
Morita et al.'s model [33]	$\Delta P_w^{cr} = \frac{1}{3-2\left(\frac{1-2\mu}{1-\mu}\right)}$ $\left( -3\bar{\sigma}_H - 2T_0 + \frac{2T_0(3+\alpha)}{\alpha} \times \left[ \left[ 1 + \frac{B_0 + 2B_1 T_0}{2T_0 \frac{1-\mu}{E} \frac{3+\alpha}{3+2\alpha} \sqrt{\frac{1}{6}(\alpha^2 + 4\alpha + 6)}} \right]^{2\alpha+3} \right] - 1 \right)$	$C_0 = \frac{3C}{\sqrt{9+12 \tan^2 \phi}}$ $C_1 = \frac{\tan \phi}{\sqrt{9+12 \tan^2 \phi}}$ $\alpha = \frac{6C_1}{\frac{1}{\sqrt{3}} - 2C_1}$ , $T_0 = \frac{C_0}{\frac{1}{\sqrt{3}} - 2C_1}$	

Vaziri et al.'s model [34]	$\Delta P_w^{cr} \leq P_0 - \frac{2\sigma_v - \lambda \times TWC}{2 - A} - P_0 \frac{A}{2 - A}$ $A = \frac{(1 - 2\mu)B}{1 - \mu}$	$\sigma_v$ is the vertical stress, $\lambda$ is a factor depending on thick-wall cylinder strength (TWC) test,
	$\Delta P_w^{cr} = (Ck + P_0) - \sqrt{(Ck + P_0)^2 - 2CkP_0};$ $k = \frac{4 \cos \phi}{1 - \sin \phi}$	$C$ is the cohesive force, $\phi$ is the frictional angle, $P_0$ is the Tensile Failure pore pressure

Numerical simulations based on the Finite Element Method (FEM), Finite Difference Method (FDM), Boundary Element Method (BEM) and Discrete Element Method (DEM) were widely used for sanding prediction coupling with the geological modeling of the reservoir [35–37]. Nouri et al. [38] coupled laboratory experiments and numerical simulation to study the time-dependent stability of the wellbore, and sand production induced by depletion, drawdown, and water-cut. Volonté et al. [39] established an ideal 3D model of the wellbore and simulated the equivalent plastic strain around the perforations for sanding prediction. Gui et al. [40] acquired the plastic strain limits modelled from advanced TWC core tests and systematic triaxial compressive core tests. They coupled this rock failure criterion and numerical simulations for sanding evaluations. Zhang et al. [25] calculated the CDP of sanding onset for offshore depleted and water cut gas reservoirs coupling with the fully-polyaxial rock failure criterion Mogi–Coulomb and FEM. Lu et al. [41] predicted the CDP of sanding onset considering the influence of drag stress, formation water production, reservoir pressure depletion, and temperature difference in the perforated wellbore in ultra-deep reservoirs. More studies of the numerical simulations on the CDP of sanding production are included in [35–37]. However, the in-situ crustal stress of the reservoir was not considered in these studies. In addition, it was usually difficult to acquire the accurate distribution of the rock properties as the target formation size increased.

The present study took a depleted gas reservoir as a potential UGS site to study the CDP of sanding production in the wellbore. Laboratory tests on the rock samples drilled from three target wells were conducted to acquire the basic rock properties. The in-situ mechanical properties of rock were estimated by coupling the laboratory test results and well-logging data. The in-situ stress field of the target formation was then deduced through inversed analysis coupled with finite element method (FEM) and genetic algorithm (GA), based on the existing known stress data and the seismic data of the measured points. The CDPs for the onset sanding production of three target wells in the UGS were predicted. The effects of the moisture content and cycling times of gas injection and withdrawal on the CDP were analyzed.

## 2. Methodology

### 2.1. Experimental Test on Mechanical Properties of Reservoir Rock

Accurate estimation of the rock properties in the target reservoir is essential for the case study on geomechanical numerical simulation. The laboratory tests were conducted to acquire the static properties including the density, porosity, permeability and mechanical properties. A depleted gas reservoir in China was chosen as the potential UGS site. A total of 40 sandstone core samples from the wells (named #1, #2 and #3) in the target reservoir were drilled and used for laboratory tests, including the density, porosity, permeability, uniaxial compression strength, cohesive strength and friction angle. The density of the tested cores was in the range 1.9 g/cm<sup>3</sup> to 2.4 g/cm<sup>3</sup>, and the porosity range was 7.8% to 27.9%; the permeability range of from 0.65 to 973.37 mD. The mechanical properties tests were performed using the MTS 815 rock mechanics test system, as shown in Figure 1a. The acquired stress-strain curve and the core images before and after the test in well #1 are presented in Figure 1b. The results indicate that the triaxial compressive strength

ranged from 55.9 MPa to 143.9 MPa, and the Poisson's ratio ranged from 0.07 to 0.19, while the Young's modulus ranged from 4.5 GPa to 9.4 GPa. As shown in Figure 1c, by fitting the maximum principal stress and confining pressure obtained by the experiment, the Mohr circle of the corresponding rock sample can be obtained, and then the friction angle and cohesion strength can be obtained.

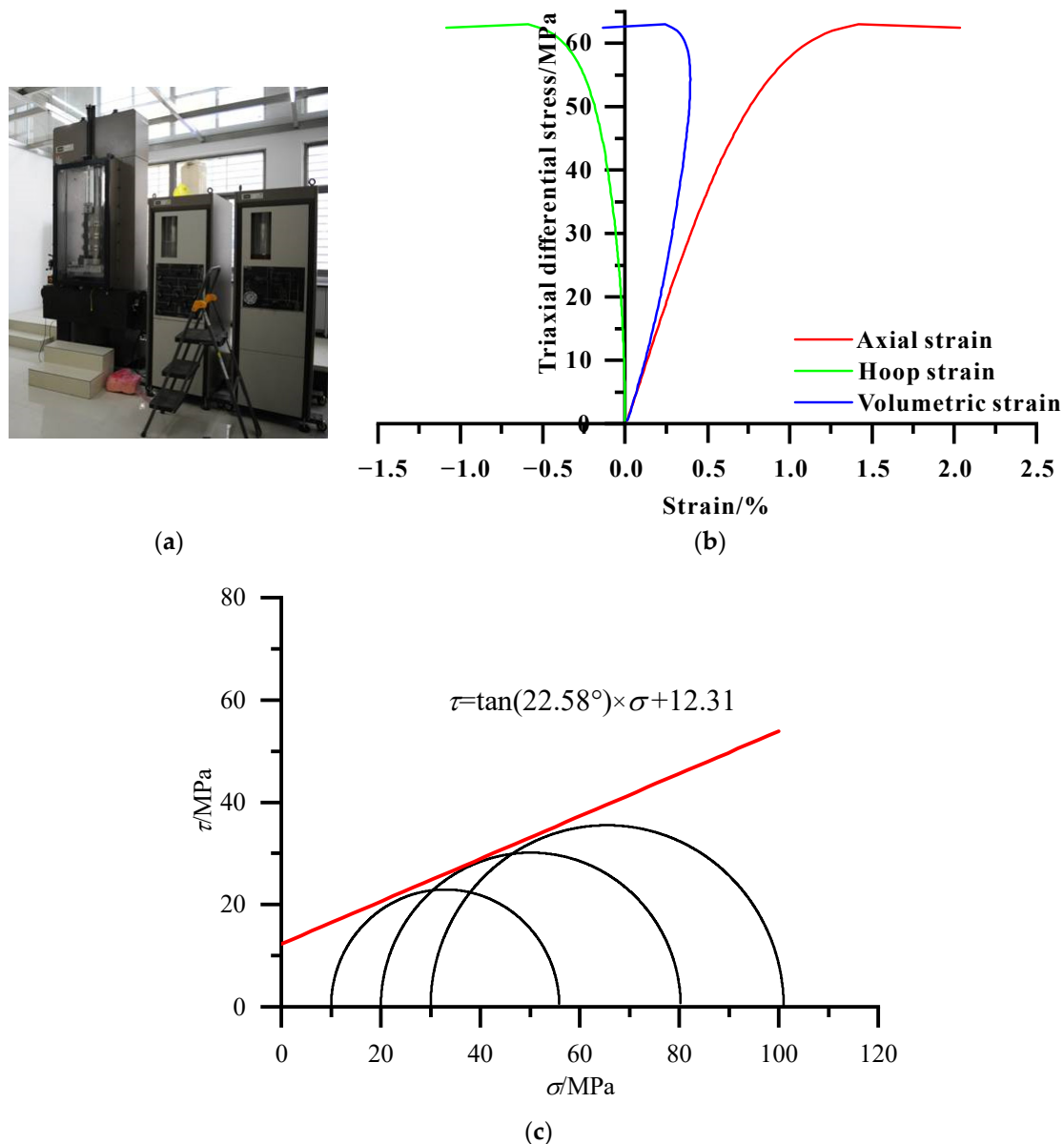


**Figure 1.** Triaxial compression test on the drilled core from the target formation. (a) MTS 815 rock mechanics test system. (b) Stress-strain curve and images before and after the test of one core sample in well #1. (c) The fitted Mohr circle and the calculation of the friction angle and cohesion strength.

The in-situ mechanical properties of rock were estimated by coupling the laboratory test results and well-logging data including the caliper (CAL), compressional sonic travel time (DTC), shear sonic travel time (DTS), gamma ray (GR), neutron porosity (NP), invaded zone resistivity (RI), flushed zone resistivity (RXO), true formation resistivity (RT) and the density logging data (DEN). The empirical correlations [42] were adopted to estimate the Poisson's Ratio, Young's Modulus, and Shear Modulus using DTS and DTC, as follows:

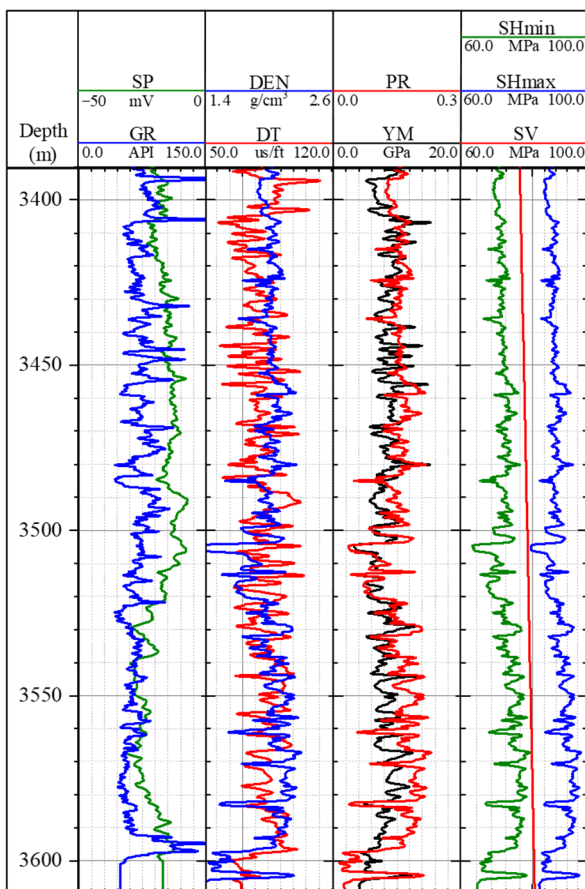
$$\mu = \frac{\Delta t_s^2 - 2\Delta t_p^2}{2(\Delta t_s^2 - \Delta t_p^2)} \tag{1}$$

$$E = \rho \frac{(1 + \mu)(1 - 2\mu)}{\Delta t_p^2(1 - \mu)} \tag{2}$$

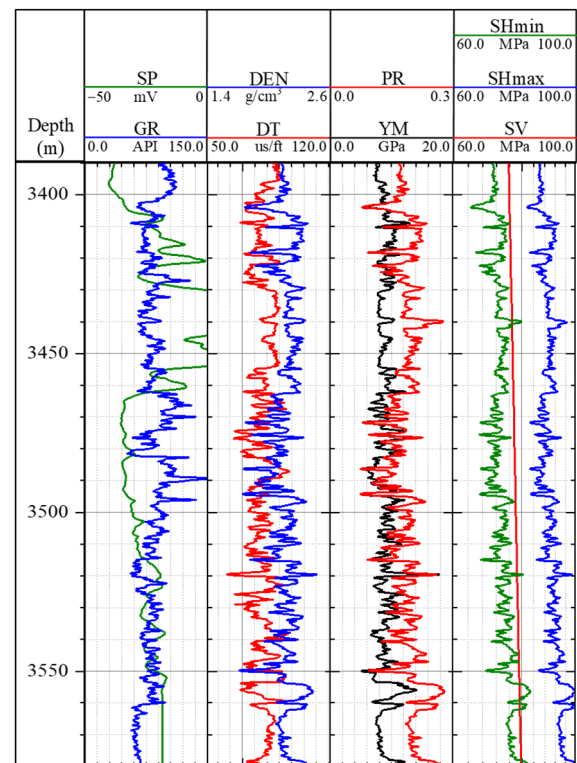
$$G = \frac{\rho}{\Delta t_s^2} \tag{3}$$

where  $E$ ,  $\mu$ , and  $G$  are the Young's Modulus (YM), the Poisson's Ratio (PR), and the Shear Modulus, respectively.  $\Delta t_p$  and  $\Delta t_s$  are the compressional sonic travel time and shear sonic travel time, respectively.

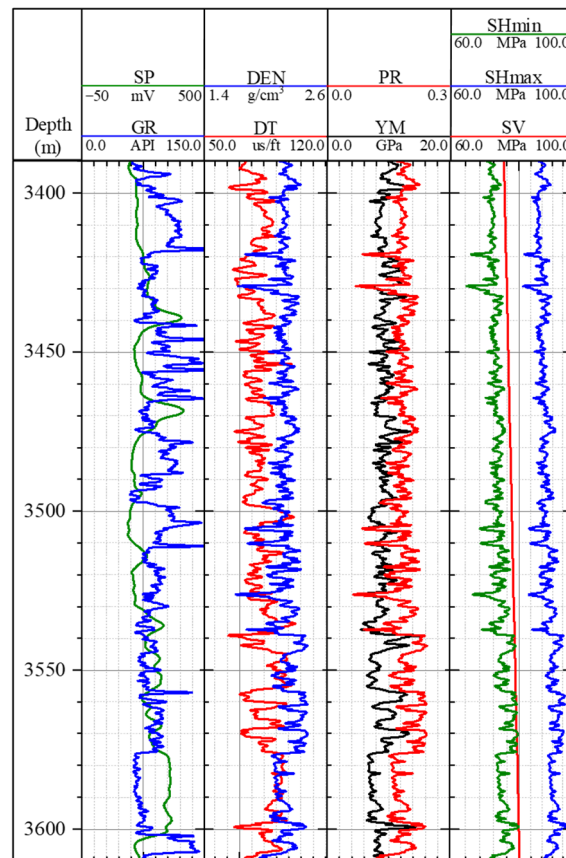
The well logging data of #1, #2 and #3 included the CAL, DTC, DTS, GR, NP, RI, RXO, RT and DEN. Then, the mechanical properties of the rock in the corresponding well were calculated using the linearly modified equations of Equations (1)–(3), as shown in Figure 2. Meanwhile, the crustal stress of the three wells (shown in Figure 3a), including the maximum horizontal principal stress ( $SH_{max}$ ), the minimum horizontal principal stress ( $SH_{min}$ ), and the vertical principal stress (SV), were estimated using the empirical equation proposed by [43]. The estimated crustal stress values of the three wells were adopted as the initial conditions for the inversed analysis of the in-situ crustal stress in the target formation in the next section, in order to improve the convergence efficiency.



(a)



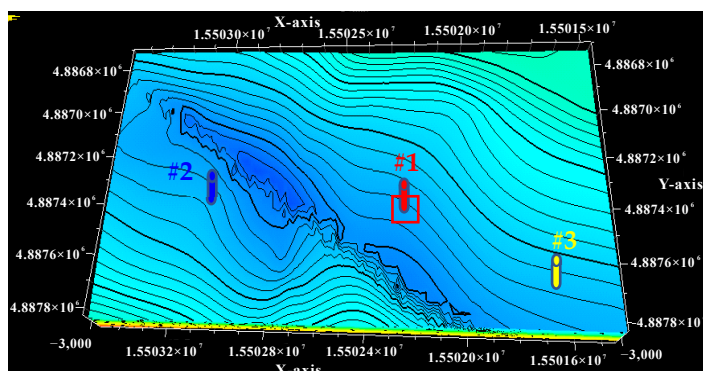
(b)



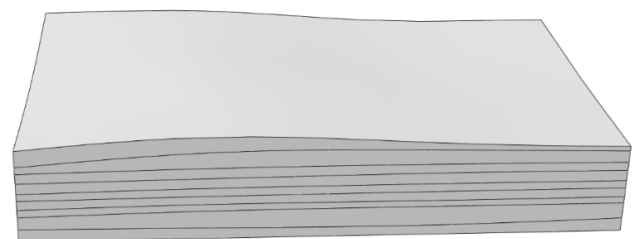
(c)

**Figure 2.** Well logging and geomechanical properties profile of the target wells. (a) Well #1. (b) Well #2. (c) Well #3.

The geological model of the reservoir horizon in the target UGS site was extracted, which was 3800 m × 1740 m on the plane and divided into 9 layers, as shown in Figure 3a. The locations of the three target wells described in this article are also marked in Figure 3a. The geological model was converted into an FEM geomechanical model using 3DMAX and Abaqus software, as shown in Figure 3b,c. Based on the mechanical properties from the well logging data, the rock properties near the well zone were initialized in the geological model. Taking the rock properties of the three wells as the restrictions, the rock properties of reservoir (e.g., the density, YM and PR) could be mapped in the extracted 3D geological model by weighted interpolation analysis method based on the seismic data and the fine geological model, as shown in Figure 4a–c.



(a)



(b)

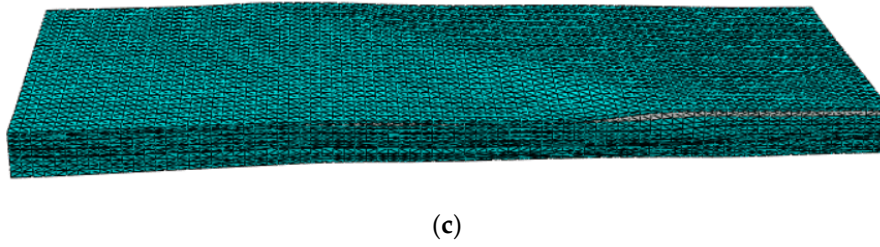


**Figure 3.** FEM geomechanical modeling of the target reservoir. (a) Geological model and well location. (b) Geometry of FEM geomechanical model. (c) FEM geomechanical model mesh.

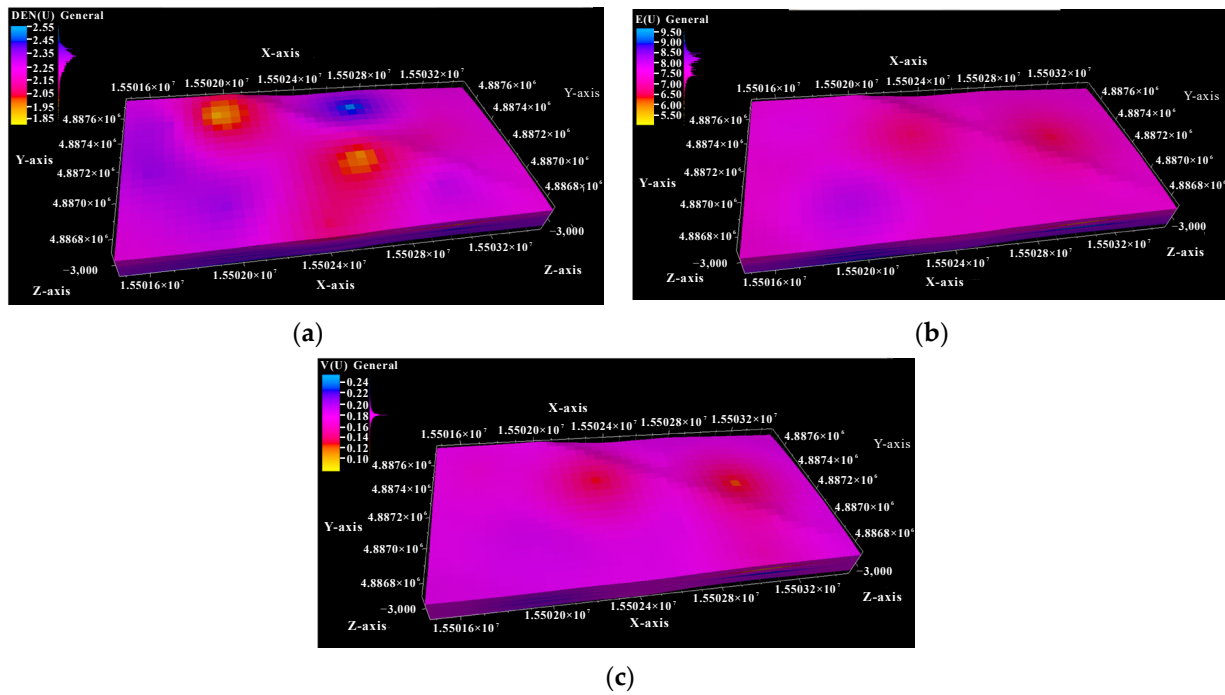


**Figure 4.** Mapped rock properties based on the FEM model of the target reservoir. (a) Density (unit: g/cm<sup>3</sup>) distribution of the target formation. (b) Young's Modulus (unit: GPa) distribution of the target formation. (c) Poisson's Ratio distribution of the target formation.

## 2.2. Mathematical Model of the Yield Criterion for Simulation

The Drucker–Prager yield criterion is adopted for the plastic deformation of rock [44],

$$\sqrt{J_2} = A + BI_1 \quad (4)$$

where  $I_1$  is the first invariant of the Cauchy stress and  $J_2$  is the second invariant of the deviatoric part of the Cauchy stress. The constants  $A$ ,  $B$  are determined from experiments. If assuming that the Drucker–Prager yield surface circumscribes the Mohr–Coulomb yield surface, then the expressions for  $A$  and  $B$  are as follows [44]:

$$A = \frac{6c \cos \phi}{\sqrt{3}(3 - \sin \phi)}$$

$$B = \frac{2 \sin \phi}{\sqrt{3}(3 - \sin \phi)} \quad (5)$$

where  $c$  and  $\phi$  are the cohesive strength and friction angle, respectively.

The equivalent plastic strain ( $\epsilon_p$ ) is adopted as the failure criterion of the rock near the wellbore [44],

$$\varepsilon_p = \sqrt{\frac{2}{3}(\varepsilon_{px}^2 + \varepsilon_{py}^2 + \varepsilon_{pz}^2)} \quad (6)$$

where  $\varepsilon_{px}$ ,  $\varepsilon_{py}$ ,  $\varepsilon_{pz}$  and are the plastic strains in the three principal stress directions, dimensionless. According to the previous studies, the well is believed to be sanding when the equivalent plastic strain exceeds the critical strain limit (CSL), which was usually defined as from 3‰ to 8‰ [30,45,46]. In this study, the CSL of 5‰ is used.

### 3. Results and Discussion

#### 3.1. Inversion of the In-Situ Stress Distribution

In this article, the in-situ stress field of the target formation was deduced through inversed analysis coupled FEM and genetic algorithm (GA), based on the existing known stress data and the seismic data of the measured points. The workflow of the inversed analysis on the in-situ stress is presented in Figure 5. In the inversed analysis, the displacement boundary variables were treated as the target parameters, and the in-situ stresses at the wellbore #1 as the objective function. The FEM geomechanical model was constructed on the ABAQUS software platform to calculate the in-situ stress state. The simulations on the stress equilibrium of FEM geomechanical model were conducted according to the initialization of the crustal stress in Section 2.1. Then, the ABAQUS software coupling the GA code via MATLAB software platform was employed to realize the reversion analysis of the in-situ crustal stress. The GA codes generated different boundary displacement loading variables and transferred them to ABAQUS for in-situ stress calculation, and then the errors were obtained by comparison with the objective function of the measured stress value of well #1. When the errors were beyond the threshold, the GA codes would generate new arrays of the inputted parameters and conduct new iterations. As shown in Figure 6, as genetic iterations increase, the error gradually decreases and it is tending towards stability when the iterations are more than 500. The inversed analysis process was regarded as being complete.

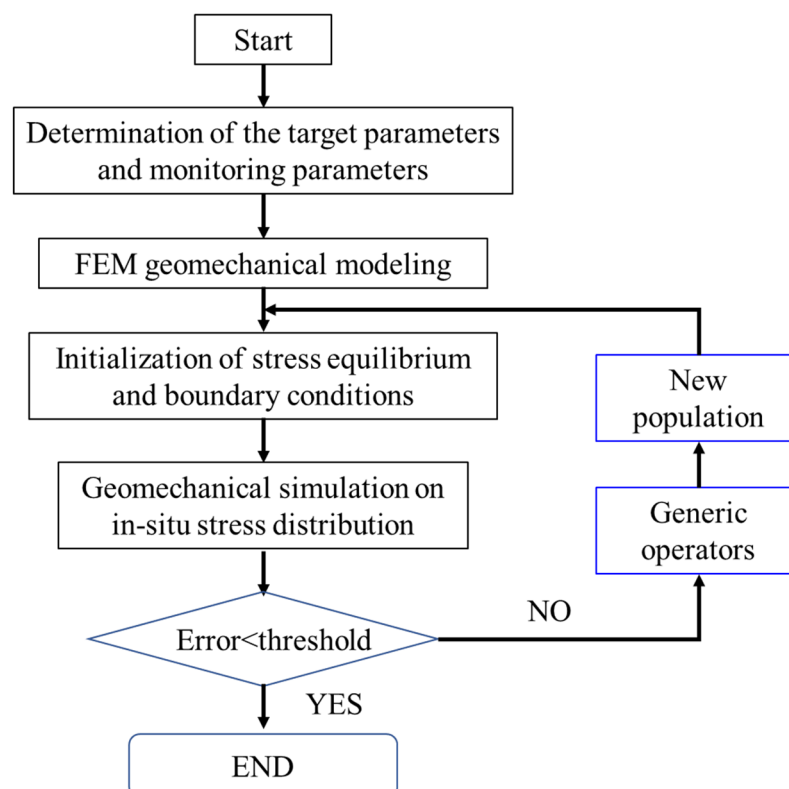
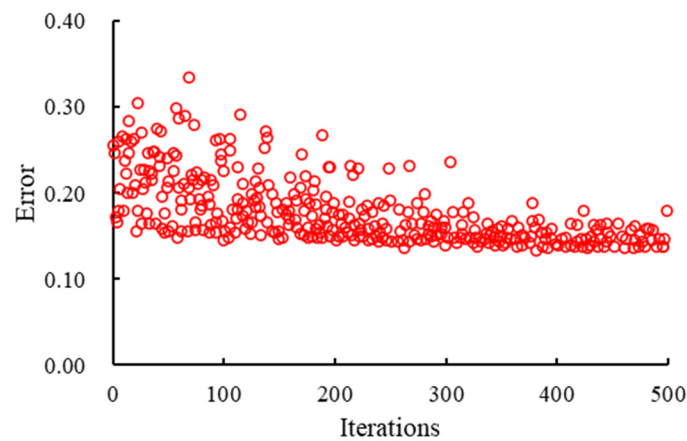
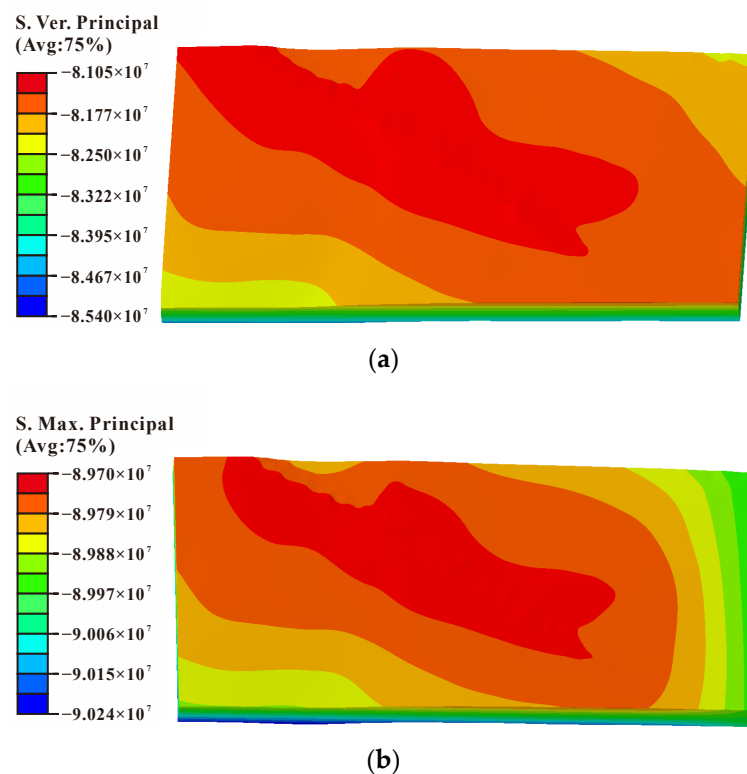


Figure 5. Reversion of in-situ geostress coupling FEM simulation with GA.



**Figure 6.** Calculation error vs. genetic iterations.

The distribution of the in-situ crustal stress after the inversion analysis is presented in Figure 7, including the vertical principal stress, maximum and minimum horizontal principal stress. The results follow the convention of elastic-plastic mechanics, that is, tensile stress is positive and compressive stress is negative. The maximum horizontal principal stress ranges from 92.6 MPa to 93.7 MPa, minimum horizontal principal stress is 67.9 MPa to 76.0 MPa and vertical principal stress is 79.4 MPa to 83.2 MPa. The direction of the maximum horizontal primary stress is in the  $x$  direction.



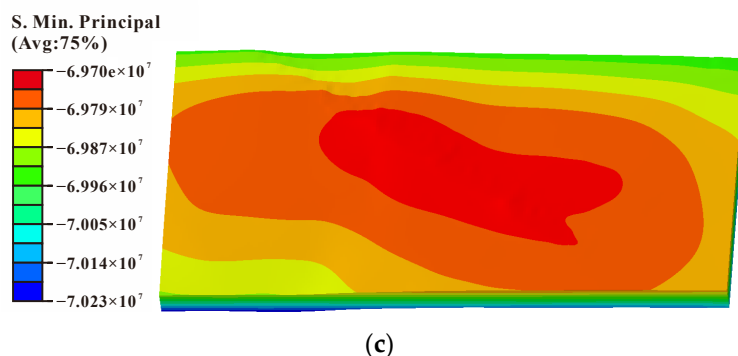


**Figure 7.** Simulation results of distribution of three principal stresses. (a) Vertical principal stress. (b) Maximum horizontal principal stress. (c) Minimum horizontal principal stress.

### 3.2. Simulation on Sanding Prediction of Well Failure in UGS

As shown in Figure 8a, three wells (named #1, #2, and #3) in the target reservoir were simulated for the sand onset prediction of well failure during the gas injection and withdrawal of the UGS. Based on the stress distribution obtained by inversed analysis, the sub model of the zone near the wellbore was established, as shown in Figure 8a. The diameter of the gas wellbore in the UGS is 99 mm, as shown in Figure 8b,c. The side length of the sub model is 2 m, about 20 times larger than the wellbore diameter, in order to reduce the boundary effect. The corresponding crustal stress distribution was extracted (as shown in Figure 8d), and then it was imposed on the sub model while the surrounding surfaces and the bottom surface were defined as fixed support. According to the Saint-Venant's principle, the equivalent treatment of the crustal stress will not change the stress distribution of the zone near a well. The stress distribution of the well #1, #2, and #3 after the equilibrium of the crustal stress was presented in Figure 9, including the equivalent stress and the stress along  $x$ ,  $y$ ,  $z$  directions. The results indicate that the maximum horizontal principal stress (in  $x$  direction) ranges from 84.6 to 91.2 MPa, the minimum horizontal principal stress (in  $y$  direction) ranges from 64.6 to 72.0 MPa, and the vertical Intermediate principal stress (in  $z$  direction) ranges from 77.8 to, 82.0 MPa. The three wells are in strike-slip stress state.

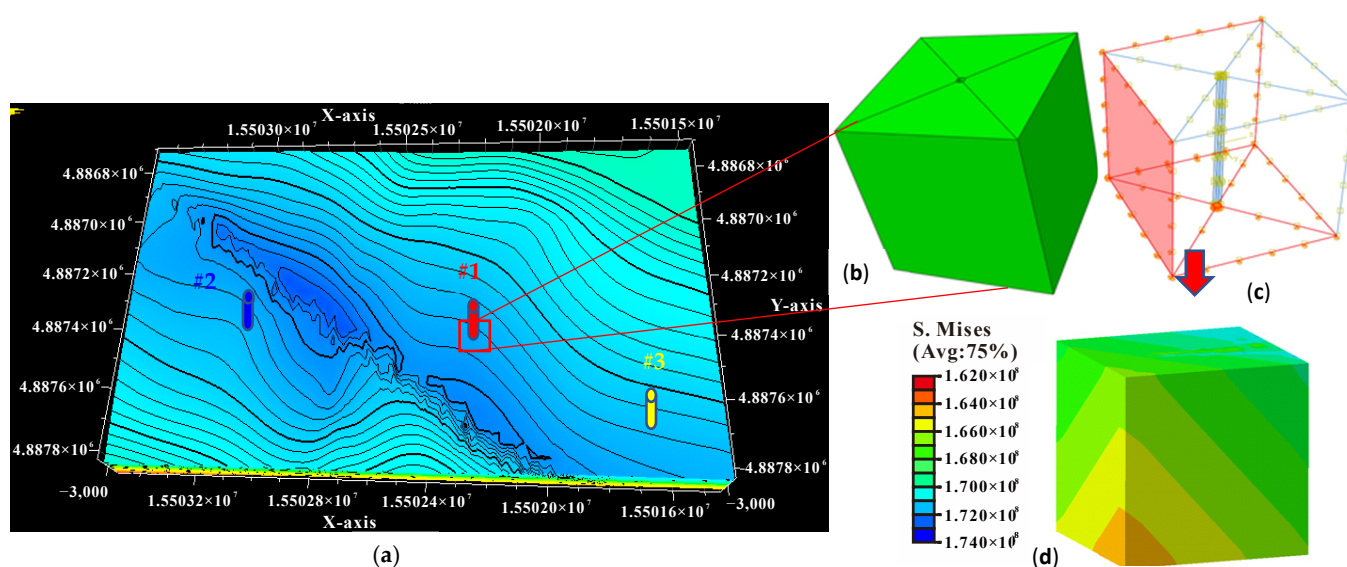


**Figure 8.** Extraction of the sub-model with stress field surrounding the target well. (a) Geological model of target formation. (b) Model of the zone near well. (c) Schematic of wellbore and boundary conditions. (d) Schematic of crustal stress for the sub

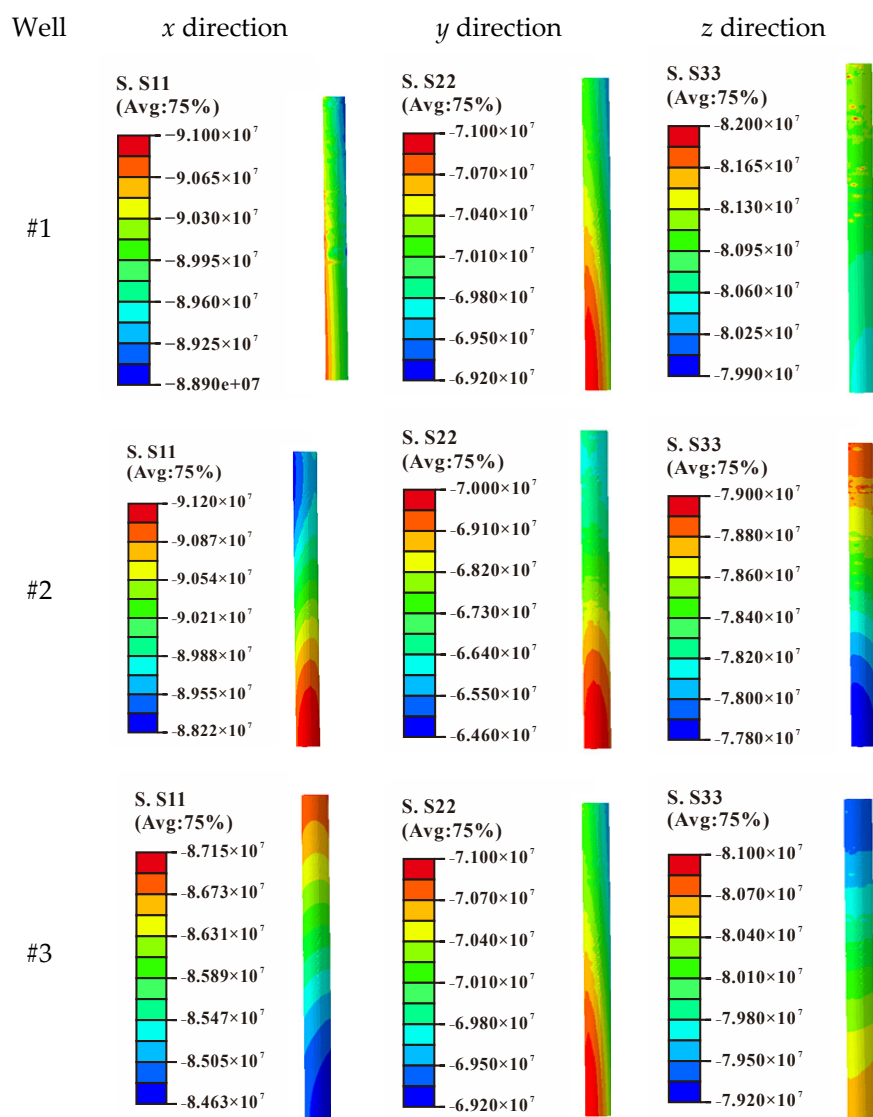
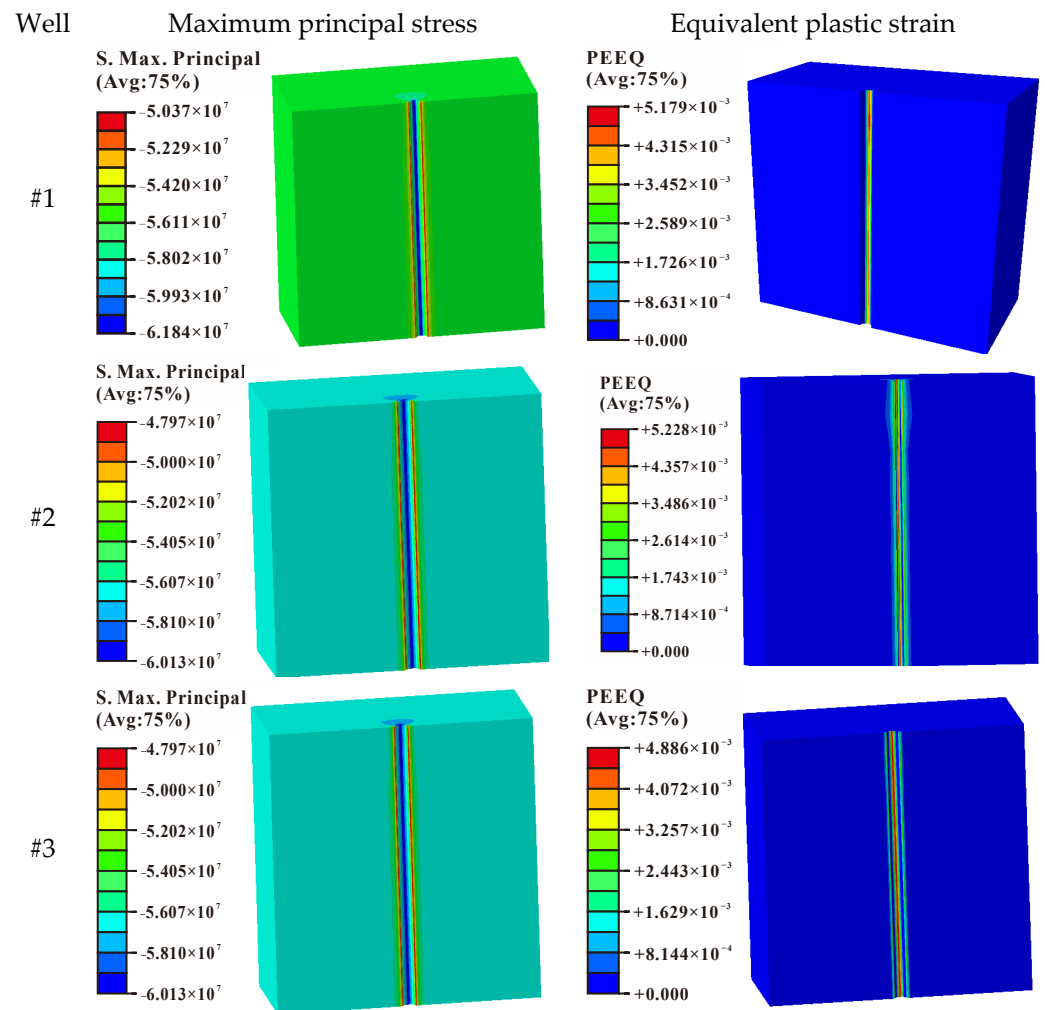


Figure 9. Stress distribution of the well zone after crustal stress initialization.

The well drilling was simulated through deactivating the wellbore elements in ABAQUS. At the same time, the static fluid column pressure (equal to the static pressure of the mud column with density of  $1.0 \text{ g/cm}^3$  at vertical height) was applied to the inner wall to ensure the stability of the wellbore and simulate the process of balanced drilling. Then the static fluid column pressure in the wellbore was decreased to simulate the gas production process. The amplitude function of the equivalent plastic strain around the wellbore was investigated. When the equivalent plastic strain exceeded the CSL, the wellbore was considered to be at high risk of sanding. The maximum principal stress and the equivalent plastic strain distribution of the wells when exceeding the CSL are presented in Figure 10. The maximum equivalent plastic strain distributed in the direction of maximum principal stress. As usual, compressive stress is negative. The corresponding differential pressures of the gas production are the critical pressure of the wellbore sanding, which are 5.59 MPa, 3.98 MPa and 4.01 MPa for well #1, well #2 and well #3 when the pressure of the gas storage is 30 MPa, respectively. During the gas injection and withdrawal of UGS, sand onset occurred at well #2 and #3 in the gas production when the differential pressure of the increased to 3.8 MPa and 4.1 MPa. The simulation results showed good agreements with the field-measured benchmark data.



**Figure 10.** Maximum principal stress and the equivalent plastic strain distribution of the wells at the CSL.

### 3.3. Influencing Factors of the Critical Pressure Difference for Sanding in UGS

The rock strength is the intrinsic factor for the critical differential pressure (CDP) of sanding in the wellbore during gas production. The experimental results showed that with the increase of moisture contents, and cycling times of gas injection and withdrawal, the rock strength of the reservoir decreases, which affects the critical sand production pressure difference of gas wells. Taking well #1 as an example, the effects of water saturation (ranging from 10% to 40%), and cycling times of gas injection and withdrawal (ranging from 40 to 200 cycling times) on the critical differential pressure were simulated and analyzed. The maximum principal stress and the equivalent plastic strain distribution of the wells for different moisture contents and cycling times when exceeding the CSL are presented in Figures 11 and 12. The maximum equivalent plastic strain distributed in the direction of maximum principal stress. The CDP for different moisture contents are presented in Figures 13 and 14. The results indicated that the CDP decreased with increase of the moisture content and the cycling times. The functional relationship between the CDP and the moisture content and the cycling times were fitted and are presented in Figures 13 and 14.

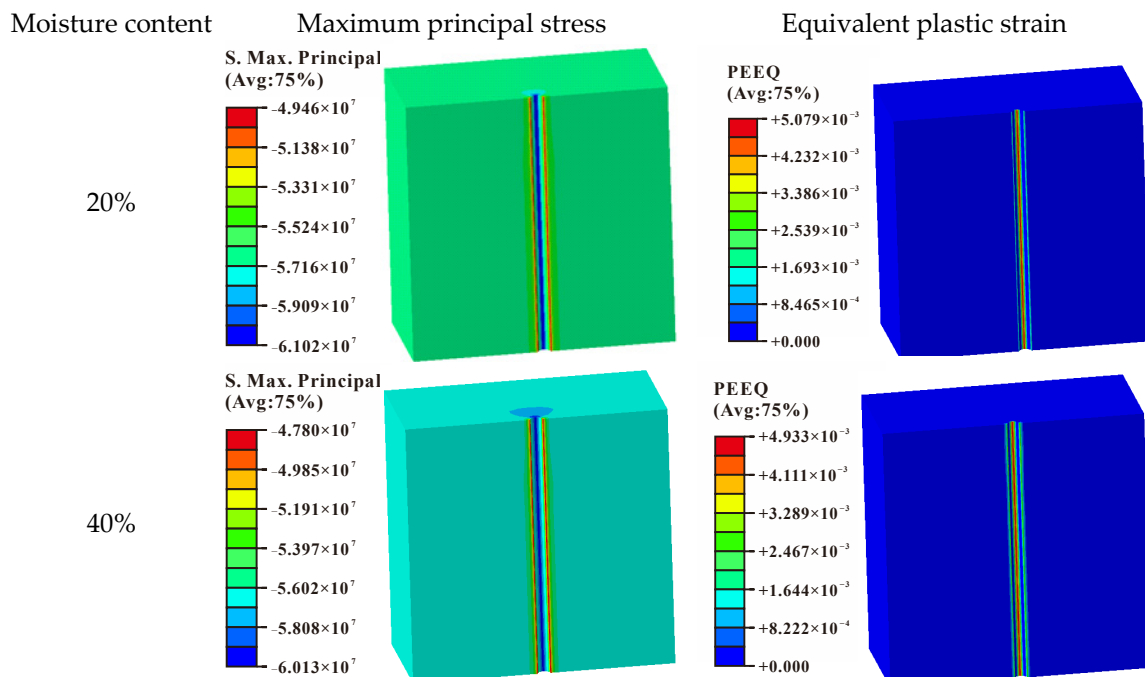


Figure 11. Maximum principal stress and the equivalent plastic strain distribution of the wells at CSL for different moisture contents.

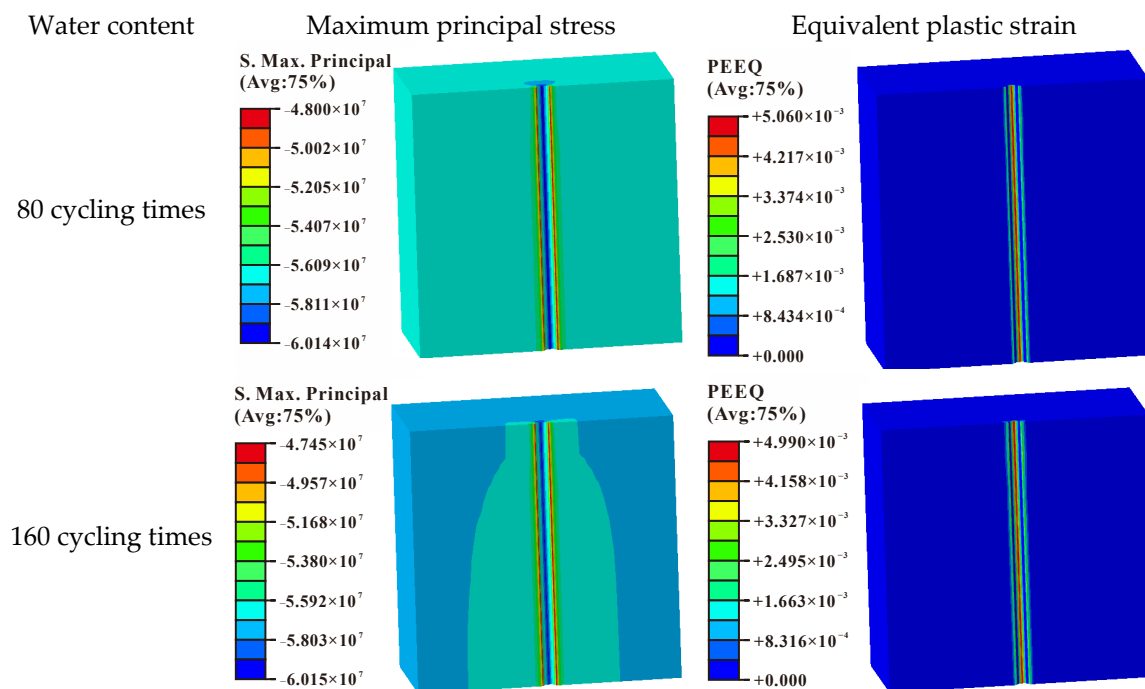
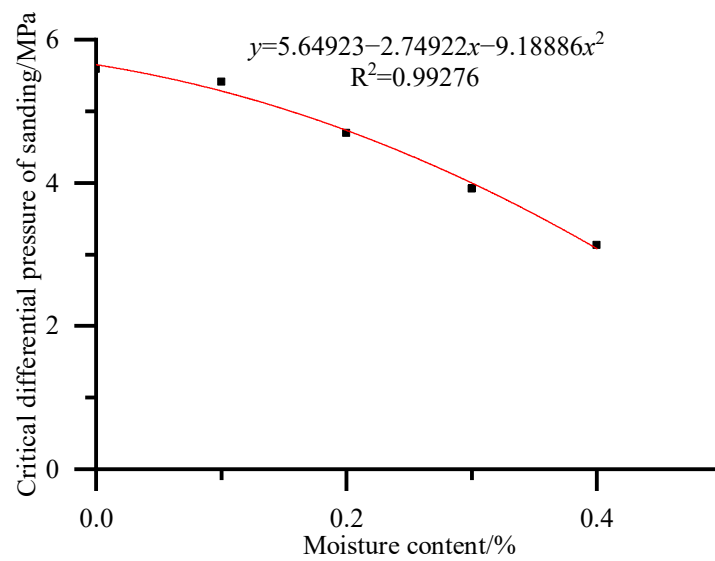
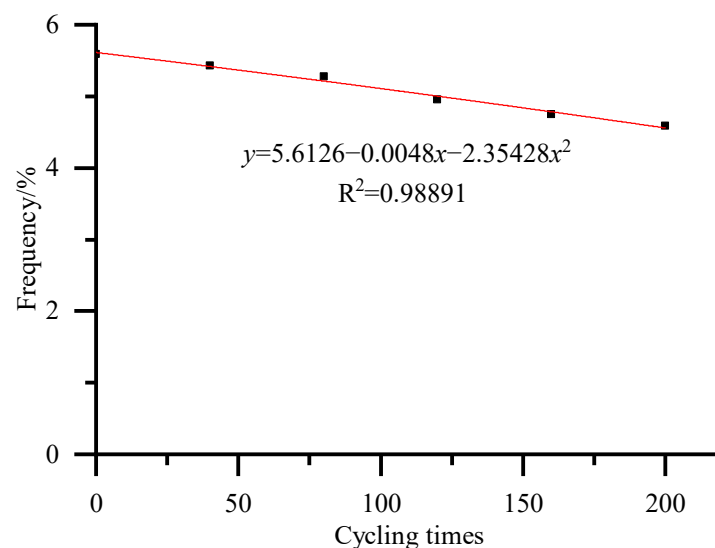


Figure 12. Maximum principal stress and the equivalent plastic strain distribution of the wells at CSL for different cycling times of gas injection and withdrawal.



**Figure 13.** Critical differential pressure of gas production for different moisture content.



**Figure 14.** Critical differential pressure of gas production for different cycling times of gas injection and production.

#### 4. Conclusions

A depleted gas reservoir was taken as the potential UGS site to investigate the CDP of sanding production in the wellbore in this study. Laboratory tests on the rock samples drilled from three target wells were conducted to acquire the basic rock properties. The in-situ mechanical properties of the rock were estimated by coupling the laboratory test results and well-logging data. The in-situ stress field of the target formation was then deduced through inversed analysis coupled finite element method (FEM) and genetic algorithm (GA), based on the existing known stress data and the seismic data of the measured points. The CDP of the wellbore in the UGS and the influencing factors were also predicted and analyzed. The following conclusions can be reached:

- (1) Based on the experimental results, the functional relationship between key rock mechanics and rock density, such as compressive strength, elastic modulus, and Poisson's ratio, was established. Coupling with the well-logging curves, the mechanical properties of the rock in the coring well could be calculated accurately.

- (2) The 3D geological model of the reservoir for UGS was transformed to a finite element geomechanics model, and was used as inputs for the inversed analysis of in-situ crustal stress. Adopting the measured in-situ stress in the samples of Well #1 as the target parameter, the crustal stress of the reservoir was determined coupling with the genetic algorithm and geomechanical simulation on Abaqus software.
- (3) Based on the stress distribution obtained by inversed analysis, the sub model of the zone near the wellbore was established. Numerical simulations on the well drilling and the cycling of high-speed injection-withdrawal were conducted. Taking the CSL of 5‰ as the sanding criterion of the wellbore, the CDPs of the gas production in the UGS were predicted, which are 5.59 MPa, 3.98 MPa, and 4.01 MPa for well #1, well #2 and well #3 when the pressure of the gas storage is 30 MPa, respectively. The simulation results showed good agreement with the field-measured benchmark data of well #2 and well #3.
- (4) The effects of moisture contents (ranging from 10% to 40%), and cycling times of gas injection and withdrawal (ranging from 40 to 200 cycling times) on the critical differential pressure were simulated and analyzed. The results indicated that the CDP decreased with increase of the moisture content and the cycling times.

This study provides a workflow of the sanding prediction coupling laboratory tests, inversed analysis with well logging data and numerical simulations, which requires plenty of drilled cores to acquire the accurate mechanical properties of the rock in the production wells of the UGS. Some testing technology based on the rock cuttings will decrease the coring and experimental costs. Meanwhile, more in-situ crustal stress data will contribute to the accuracy of the CDP prediction.

**Author Contributions:** Conceptualization, R.S.; Data curation, R.S., P.Z. and X.T.; Funding acquisition, R.S.; Investigation, J.L.; Software, F.H.; Validation, Z.L.; Visualization, Z.L.; Writing—original draft, J.L.; Writing—review & editing, J.L. All authors have read and agreed to the published version of the manuscript.

**Funding:** This research was funded by [Knowledge Innovation Program of Wuhan-Basic Research] grant number [2022010801010158]. The APC was funded by [Knowledge Innovation Program of Wuhan-Basic Research].

**Institutional Review Board Statement:** Not applicable.

**Informed Consent Statement:** Not applicable.

**Data Availability Statement:** All the data and materials used in this paper are available from the corresponding author upon request.

**Acknowledgments:** This work was financially supported by Knowledge Innovation Program of Wuhan-Basic Research (2022010801010158).

**Conflicts of Interest:** The authors declare that they have no known competing financial interest or personal relationships that could have appeared to influence the work reported in this paper.

## Abbreviations

3D	Three dimensional
ATWC	Advanced thick-walled cylinder ()
BEM	Boundary Element Method
CSL	Critical strain limit
CDP	Critical differential pressure
DEM	Discrete Element Method
FDM	Finite Difference Method
FEM	Finite element method
GA	Genetic algorithm
NG	Natural gas
PR	Poisson's Ratio
TWC	Thick-wall cylinder strength

UCS	Unconfined compressive strength
UGS	Underground gas storage
YM	Young's Modulus

## References

- Song, R.; Cui, M.; Liu, J. Single and multiple objective optimization of a natural gas liquefaction process. *Energy* **2017**, *124*, 19–28. <https://doi.org/10.1016/j.energy.2017.02.073>.
- Song, R.; Sun, S.; Liu, J.; Yang, C. Pore scale modeling on dissociation and transportation of methane hydrate in porous sediments. *Energy* **2021**, *237*, 121630. <https://doi.org/10.1016/j.energy.2021.121630>.
- Song, R.; Liu, J.; Yang, C.; Sun, S. Study on the multiphase heat and mass transfer mechanism in the dissociation of methane hydrate in reconstructed real-shape porous sediments. *Energy* **2022**, *254*, 124421. <https://doi.org/10.1016/j.energy.2022.124421>.
- Ali, A. Data-driven based machine learning models for predicting the deliverability of underground natural gas storage in salt caverns. *Energy* **2021**, *229*, 120648. <https://doi.org/10.1016/j.energy.2021.120648>.
- Gümrah, F.; Katircioglu, D.; Aykan, Y.; Okumus, S.; Kilincer, N. Modeling of gas demand using degree-day concept: Case study for Ankara. *Energy Sources* **2001**, *23*, 101–114.
- Verga, F. What's conventional and what's special in a reservoir study for underground gas storage. *Energies* **2018**, *11*, 1245.
- Matos, C.R.; Carneiro, J.F.; Silva, P.P. Overview of large-scale underground energy storage technologies for integration of renewable energies and criteria for reservoir identification. *J. Energy Storage* **2019**, *21*, 241–258.
- Confort, M.J.F.; Mothe, C.G. Estimating the required underground natural gas storage capacity in Brazil from the gas industry characteristics of countries with gas storage facilities. *J. Nat. Gas Sci. Eng.* **2014**, *18*, 120–130. <https://doi.org/10.1016/j.jngse.2014.02.004>.
- Arfaee, M.I.R.; Sola, B.S. Investigating the effect of fracture–matrix interaction in underground gas storage process at condensate naturally fractured reservoirs. *J. Nat. Gas Sci. Eng.* **2014**, *19*, 161–174. <https://doi.org/10.1016/j.jngse.2014.05.007>.
- Vilarrasa, V.; De Simone, S.; Carrera, J.; Villaseñor, A. Unraveling the causes of the seismicity induced by underground gas storage at Castor, Spain. *Geophys. Res. Lett.* **2021**, *48*, e2020GL092038.
- Schultz, R.A.; Evans, D.J. Occurrence frequencies and uncertainties for US underground natural gas storage facilities by state. *J. Nat. Gas Sci. Eng.* **2020**, *84*, 103630. <https://doi.org/10.1016/j.jngse.2020.103630>.
- Zhang, S.; Yan, Y.; Sheng, Z.; Yan, X. Uncertainty failure risk quantitative assessments for underground gas storage near-well-bore area. *J. Energy Storage* **2021**, *36*, 102393. <https://doi.org/10.1016/j.est.2021.102393>.
- McNulty, J.W. *An Experimental Study of Arching in Sand (No. 1)*; Waterways Experiment Station: Vicksburg, MS, USA, 1965.
- Clearly, M.P.; Melvan, J.J.; Kohlhaas, C.A. The Effect of Confining Stress and Fluid Properties on Arch Stability in Unconsolidated Sands. In Proceedings of the SPE Annual Technical Conference and Exhibition, Las Vegas, NV, USA, 23–26 September 1979.
- Tippie, D.B.; Kohlhaas, C.A. Effect of Flow Rate on Stability of Unconsolidated Producing Sands. In Proceedings of the Fall Meeting of the Society of Petroleum Engineers of AIME, Las Vegas, NV, USA, 30 September–3 October 1973.
- Ranjith, P.; Perera, M.; Perera, W.; Wu, B.; Choi, S. Effective parameters for sand production in unconsolidated formations: An experimental study. *J. Pet. Sci. Eng.* **2013**, *105*, 34–42. <https://doi.org/10.1016/j.petrol.2013.03.023>.
- Hall, C.J.; Harrisberger, W.H. Stability of Sand Arches: A Key to Sand Control. *J. Pet. Technol.* **1970**, *22*, 821–829. <https://doi.org/10.2118/2399-pa>.
- Rahman, K.; Khaksar, A.; Kayes, T.J. Minimizing Sanding Risk by Optimizing Well and Perforation Trajectory Using an Integrated Geomechanical and Passive Sand-Control Approach. In Proceedings of the SPE Annual Technical Conference and Exhibition, Denver, CO, USA, 21–24 September 2008.
- Cook, J.M.; Bradford, I.D.R.; Plumb, R.A. A study of the physical mechanisms of sanding and application to sand production prediction. In Proceedings of the European Petroleum Conference, London, UK, 25–27 October 1994.
- Bianco, L.C.B.; Halleck, P.M. Mechanisms of arch instability and sand production in two-phase saturated poorly consolidated sandstones. In Proceedings of the SPE European Formation Damage Conference, The Hague, The Netherlands, 21–22 May 2001.
- Honari, S.; Seyed Hosseinia, E. Particulate Modeling of Sand Production Using Coupled DEM-LBM. *Energies* **2021**, *14*, 906.
- Al-Shaabi, S.K.; Al-Ajmi, A.M.; Al-Wahaibi, Y. Three dimensional modeling for predicting sand production. *J. Pet. Sci. Eng.* **2013**, *109*, 348–363.
- Arbelaez-Londoño, A.; Osorio, G.; Alzate-Espinosa, G. The Wormholes Formation During the Cold Heavy Oil Production with Sand (CHOPS). In Proceedings of the ISRM 8th International Symposium Geomechanics, Bucaramanga, Colombia, 6–10 May 2019.
- Veeken, C.A.M.; Davies, D.R.; Kenter, C.J.; Kooijman, A.P. Sand production prediction review: Developing an integrated approach. In Proceedings of the SPE Annual Technical Conference and Exhibition, Dallas, TX, USA, 6–9 October 1991.
- Zhang, R.; Shi, X.; Zhu, R.; Zhang, C.; Fang, M.; Bo, K.; Feng, J. Critical drawdown pressure of sanding onset for offshore depleted and water cut gas reservoirs: Modeling and application. *J. Nat. Gas Sci. Eng.* **2016**, *34*, 159–169. <https://doi.org/10.1016/j.jngse.2016.06.057>.
- Ou, Q.; Yang, J.; Zhang, Z.; Liu, L.; Qu, X.; Hong, Y. Prediction of high-temperature and high-pressure well sand production in the DF gas field. In Proceedings of the 55th US Rock Mechanics/Geomechanics Symposium, Virtual, 18–25 June 2021.

27. Zhou, S.; Sun, F. *Sand Production Management for Unconsolidated Sandstone Reservoirs*; Petroleum Industry Press: Beijing, China, 2016. <https://doi.org/10.1002/9781118961865>.
28. Song, R.; Wang, Y.; Ishutov, S.; Zambrano-Narvaez, G.; Hodder, K.J.; Chalaturnyk, R.J.; Sun, S.; Liu, J.; Gamage, R.P. A Comprehensive Experimental Study on Mechanical Behavior, Microstructure and Transport Properties of 3D-printed Rock Analogs. *Rock Mech. Rock Eng.* **2020**, *53*, 5745–5765. <https://doi.org/10.1007/s00603-020-02239-4>.
29. Zuloaga, P.; Yu, W.; Miao, J.; Sepehrnoori, K. Performance evaluation of CO<sub>2</sub> Huff-n-Puff and continuous CO<sub>2</sub> injection in tight oil reservoirs. *Energy* **2017**, *134*, 181–192.
30. Deng, J.; Wang, L.; Li, P.; Zhao, W. The Critical Pressure Difference Prediction of Sand Production in Deepwater Sandstone Gas Reservoirs. *Pet. Sci. Technol.* **2013**, *31*, 1925–1932. <https://doi.org/10.1080/10916466.2011.553648>.
31. Nordgren, R.P. Strength of well completions. In Proceedings of the 18th US Symposium on Rock Mechanics (USRMS), Golden, CO, USA, 22–24 June 1977.
32. Almisned, O.A. A Model for Predicting Sand Production from Well Logging Data. Ph.D. Thesis, The University of Oklahoma, Norman, OK, USA, 1995.
33. Morita, N.; Whitfill, D.L.; Fedde, O.P.; Lovik, T.H. Parametric Study of Sand-Production Prediction: Analytical Approach. *SPE Prod. Eng.* **1989**, *4*, 25–33. <https://doi.org/10.2118/16990-pa>.
34. Vaziri, H.; Barree, B.; Xiao, Y.; Palmer, I.; Kutas, M. What is the magic of water in producing sand? In Proceedings of the SPE Annual Technical Conference and Exhibition, San Antonio, TX, USA, 29 September–2 October 2002.
35. Rahmati, H.; Jafarpour, M.; Azadbakht, S.; Nouri, A.; Vaziri, H.; Chan, D.; Xiao, Y. Review of Sand Production Prediction Models. *J. Pet. Eng.* **2013**, *2013*, 864981. <https://doi.org/10.1155/2013/864981>.
36. Ranjith, P.G.; Perera, M.S.A.; Perera, W.K.G.; Choi, S.K.; Yasar, E. Sand production during the extrusion of hydrocarbons from geological formations: A review. *J. Pet. Sci. Eng.* **2014**, *124*, 72–82.
37. Subbiah, S.K.; Samsuri, A.; Mohamad-Hussein, A.; Jaafar, M.Z.; Chen, Y.R.; Kumar, R.R. Root cause of sand production and methodologies for prediction. *Petroleum* **2021**, *7*, 263–271. <https://doi.org/10.1016/j.petilm.2020.09.007>.
38. Nouri, A.; Vaziri, H.; Kuru, E.; Islam, R. A comparison of two sanding criteria in physical and numerical modeling of sand production. *J. Pet. Sci. Eng.* **2006**, *50*, 55–70. <https://doi.org/10.1016/j.petrol.2005.10.003>.
39. Volonté, G.; Scarfato, F.; Brignoli, M. Sand prediction: A practical finite-element 3D approach for real field applications. *SPE Prod. Oper.* **2013**, *28*, 95–108.
40. Gui, F.; Khaksar, A.; Van Zee, W.; Cadogan, P. Improving the Sanding Evaluation Accuracy by Integrating Core Tests, Field Observations and Numerical Simulation. In Proceedings of the SPE Asia Pacific Oil & Gas Conference and Exhibition, Perth, Australia, 25–27 October 2016. <https://doi.org/10.2118/182499-ms>.
41. Lu, Y.; Xue, C.; Liu, T.; Chi, M.; Yu, J.; Gao, H.; Xu, X.; Li, H.; Zhuo, Y. Predicting the critical drawdown pressure of sanding onset for perforated wells in ultra-deep reservoirs with high temperature and high pressure. *Energy Sci. Eng.* **2021**, *9*, 1517–1529. <https://doi.org/10.1002/ese3.922>.
42. Cornelio, J.; Ershaghi, I. A Machine Learning Approach for Predicting Rock Brittleness from Conventional Well Logs. In Proceedings of the SPE Eastern Regional Meeting, Charleston, WV, USA, 15–17 October 2019. <https://doi.org/10.2118/196572-ms>.
43. Jingen, D.; Kangping, W.; Rongzun, H. In-situ stress determination at great depth by using acoustic emission technique. In Proceedings of the 35th US Symposium on Rock Mechanics (USRMS), Reno, NV, USA, 5–7 June 1995.
44. Park, S.-H.; Bang, K.-H.; Cho, J.-R. Structural Integrity Evaluation of a Reactor Cavity during a Steam Explosion for External Reactor Vessel Cooling. *Energies* **2021**, *14*, 3605. <https://doi.org/10.3390/en14123605>.
45. Santana, C.; Likrama, F. Workflow on Incorporating Thick-Walled Cylinder Test Results in Finite Element Models of near Well-bore for Sanding Prediction Studies. In Proceedings of the 50th US Rock Mechanics/Geomechanics Symposium, Houston, TX, USA, 26–29 June 2016.
46. Deng, F.; Yan, C.; Jia, S.; Chen, S.; Wang, L.; He, L. Influence of Sand Production in an Unconsolidated Sandstone Reservoir in a Deepwater Gas Field. *J. Energy Resour. Technol.* **2019**, *141*, 092904. <https://doi.org/10.1115/1.4043132>.